Lateral Confinement in 2D Nanoplatelets: A Strategy to Expand the Colloidal Quantum Engineering Toolbox

Leonardo Curti, Corentin Dabard, Lina Makké, Ningyuan Fu, Henri Lehouelleur, Muchuan Hua, Erwan Bossavit, Mariarosa Cavallo, Xiang Zhen Xu, Debora Pierucci, et al.

ADVANCED OPTICAL MATERIALS
www.advopticalmat.de

Lateral Confinement in 2D Nanoplatelets: A Strategy to Expand the Colloidal Quantum Engineering Toolbox

*Leonardo Curti, Corentin Dabard, Lina Makké, Ningyuan Fu, Henri Lehouelleur, Muchuan Hua, Erwan Bossavit, Mariarosa Cavallo, Xiang Zhen Xu, Debora Pierucci, Mathieu G. Silly, Burak Guzelturk, Emmanuel Lhuillier, Juan I. Climente, Benjamin T. Diroll, and Sandrine Ithurria**

Among colloidal nanocrystals, 2D nanoplatelets offer a unique set of properties with exceptionally narrow luminescence and low lasing thresholds. Furthermore, their anisotropic shape expands the playground for the complex design of heterostructures where spectra but also scattering rates can be engineered. A challenge that still remains is to combine shell growth which makes NPLs stable, with spectral tunability. Indeed, most reported shelled nanoplatelets end up being red emitters due to a loss of quantum confinement. Here, the combination of both lateral and in-plane confinements within a single heterostructure is explored. A CdS/CdSe/CdS/CdZnS core–crown–crown shell structure that enables yellow emission is grown and that is responsive to a large range of excitation including visible photons, X-ray photons, electron beams, and electrical excitations. *k.p* simulations predict that emission tunability of up to several 100 s of meV can be obtained in ideal structures. This material also displays stimulated emission resulting from bi-exciton emission with a low threshold. Once integrated into an LED stack, this material is compatible with sub-bandgap excitation and exhibits high luminance. Scaling of the electroluminescence properties by downsizing the pixel size is also investigated.

1. Introduction

Colloidal nanocrystals are semiconductor nanoparticles with size-tunable optical features, generating bright luminescence that sparks interest for applications ranging from single-photon sources to down-conversion for displays and lighting. In comparison to other light emitters, a key property is color purity, which, in the case of colloidal nanocrystals, is generally driven by the size polydispersity.[1] Ideal synthesis procedures should lead to single particle size, a property achieved when growing 2D nanoplatelets[2–4] (NPLs) of cadmium-based chalcogenides. The roughness-free surface of the NPLs makes it interesting to study growth mechanisms[5,6] and ligand grafting. This further leads to exceptional optical features such as the narrowest photoluminescence signal among nanocrystals, while their large volume tends to reduce Auger recombination, generating large optical gain,[7] and low-threshold lasing.[8,9]

L. Curti, C. Dabard, L. Makké, N. Fu, H. Lehouelleur, X. Z. Xu, S. Ithurria
Laboratoire de Physique et d'Etude des Matériaux
ESPCI, PSL Research University
Sorbonne Université
CNRS
10 rue Vauquelin, Paris 75005, France
E-mail: Sandrine.ithurria@espci.fr

M. Hua, B. T. Diroll
Center for Nanoscale Materials
Argonne National Laboratory
9700 S. Cass Avenue, Lemont, IL 60439, USA

The ORCID identification number(s) for the author(s) of this article can be found under https://doi.org/10.1002/adom.202400555

DOI: 10.1002/adom.202400555

E. Bossavit, M. G. Silly
Synchrotron SOLEIL
L'Orme des Merisiers
Départementale 128, Saint-Aubin 91190, France

E. Bossavit, M. Cavallo, D. Pierucci, E. Lhuillier
Sorbonne Université
CNRS
Institut des NanoSciences de Paris
4 place jussieu, Paris 75005, France

B. Guzelturk
X-Ray Science Division
Argonne National Laboratory
9700 S. Cass Avenue, Lemont, IL 60439, USA

J. I. Climente
Departament de Quimica Fisica i Analitica
Universitat Jaume I
Castello de la Plana E-12080, Spain

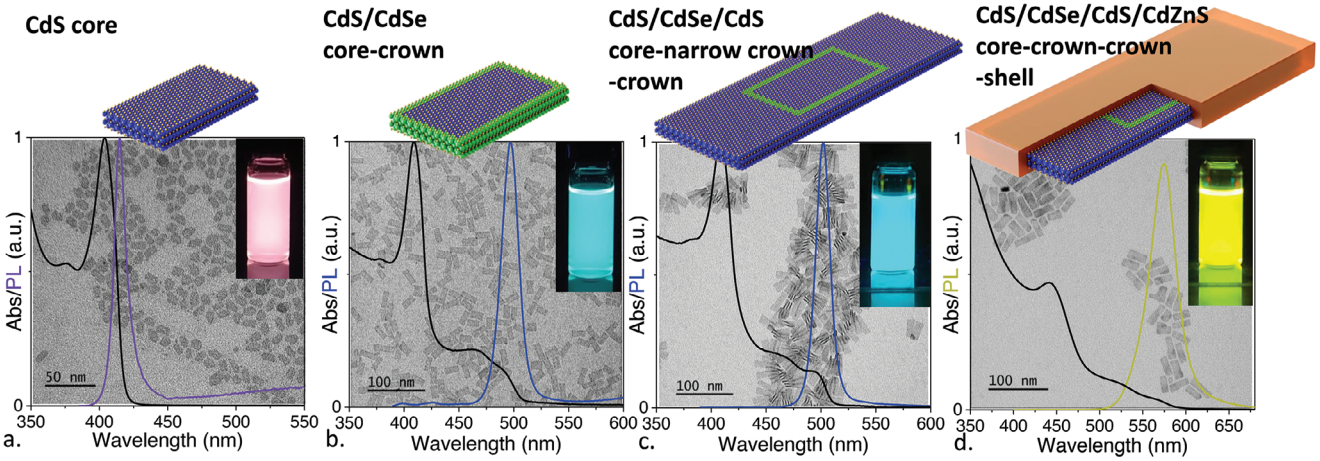

Figure 1. Synthesis of laterally confined C–C–C–S NPLs. a) Absorbance and photoluminescence spectra of CdS core NPLs (schematized on top). b) Absorbance and photoluminescence spectra of CdS/CdSe core–crown NPLs (schematized on top). c) Absorbance and photoluminescence spectra of CdS/CdSe/CdS C–C–C NPLs (schematized on top). Inset is an image of the solution under UV illumination. d) Absorbance and photoluminescence spectra of CdS/CdSe/CdS/CdZnS C–C–C–S NPLs (schematized on top). Inset is an image of the solution under UV illumination. See Table S1 (Supporting Information) for a quantitative analysis of the PL.

In order to be used as functional materials, NPLs also need spectral tunability and high stability. The spectral tunability in NPLs can simply be obtained thanks to quantum confinement, where thicker NPLs display redder features. NPLs with thicknesses of 2, 3, 4,[10] 5, 6,[11,12] and up to 11[13] monolayers have then been reported. This still limits spectral tunability to discrete steps. Alternatively, changes in color can be obtained from the growth of a heterostructure. In particular, type II band alignment[14,15] enables the design of an effective bandgap narrower than the one of either base materials. Doping[16–18] of NPLs, as well as the control of their composition[19] beyond Cd,[20] are also proven methods to cover a large spectral range.

Meanwhile, advanced control of NPL growth has enabled the growth of complex heterostructures[21–24] combining both crown (i.e., in-plane growth) and shell (i.e., isotropic growth) with new functionalities such as photon up-conversion[25] or multicolor emission.[26,27] However, in current structures, high thermal, chemical, or photonic stability always requires external shell growth. The latter reduces confinement and ends up generating red-only emission. Here, we explore how the 2D geometry enables the reconciliation of traditional thickness confinement with in-plane confinement. *k.p* simulation predicts that in ideal structures with sharp CdS/CdSe interfaces a large spectral tunability of up to 400 meV may be achieved. We successfully synthesized core–crown–crown (C–C–C) as well as core–crown–crown–shell (C–C–C–S) structures presenting a yellow emission, which can be activated through photoluminescence, radioluminescence, cathodoluminescence, as well as electroluminescence. Stimulated emission resulting from biexcitons is demonstrated, and finally, we discuss the scaling law of the electroluminescence with the pixel size reduction.

2. Results and Discussion

NPLs are intrinsically anisotropic objects in which the thickness is significantly reduced compared to the in-plane extension. As a result, core-only NPLs appear poorly suited to include lateral confinement. Nucleation and growth of very small NPLs in which confinement is expected is challenging with existing syntheses limited to ≈5 nm lateral dimensions.[28] Inspired by work on quantum dots with the emitting material grown as a shell,[29–31] we design a core–crown structure where the emitting material is the crown rather than the core. Here, we choose CdSe as the emitting material and place it in between a CdS core and a CdS external crown to form a CdS/CdSe/CdS C–C–C structure. To do so, we start with a small CdS core with a 7.5 × 12 nm^2 lateral extension and a 4.5 ML thickness. The strong thickness confinement in this NPL results in light emission at 3 eV (413 nm, see **Figure 1a**), while bulk CdS is expected to have a 2.4 eV bandgap.

Lateral confinement effects are hardly observed in homostructures due to the difficulty of synthesizing very small NPLs (particularly NPLs with a diameter smaller than 5 nm). On the contrary, the fine control of a crown's lateral growth enables precise modulation of the lateral confinement, improving the tunability of the final product's bandgap. Here, we have grown a narrow CdSe crown with a 1 nm lateral extension. The resulting absorption spectrum (Figure 1b) preserves the features of the CdS core together with new features at ≈2.48 eV (500 nm) attributed to the CdSe crown. The photoluminescence (PL) is now shifted to a wavelength matching the absorption feature from CdSe due to the type I band alignment between the two materials. The addition of a second CdS crown, by a slow controlled injection of precursors, barely affects the absorption spectrum, though it reduces the relative weight of the CdSe features. The PL also remains mostly unchanged at ≈500 nm, see Figure 1c. This value is clearly blueshifted with respect to core-only CdSe NPLs with the same thickness (or CdS/CdSe core/crown structures with larger CdSe crowns), for which the PL signal appears at 2.42 eV (512 nm), which is a good signature of lateral confinement. Finally, we grow a CdZnS shell (95% Zn nominally) to enhance the material's stability, which further redshifts both absorption and PL spectra due to the reduced vertical confinement despite type I band alignment, see Figure 1d. The PL signal also broadens as the NPLs get heterostructured, with a final full width at half maximum at

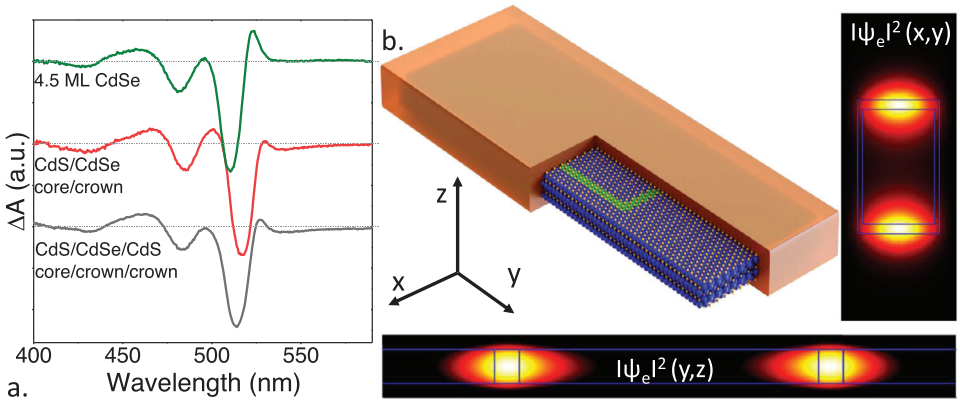

Figure 2. Electronic structure of the CdS/CdSe/CdS C–C–C NPL. a) Transient absorption spectra acquired at 1 ns after pumping at 400 nm for CdS core NPL, CdS/CdSe core crown NPL, and CdS/CdSe/CdS C–C–C NPLs. b) Schematic of the CdS/CdSe/CdS/ZnS C–C–C–S NPL and electron density within the lateral extension and the thickness.

≈37 nm, a value clearly above the value reported for core--only NPL (12 nm for the CdS core here), but at the benefit of an improved PLQY now reaching 68%. In Figure S1 (Supporting Information), a similar set of data obtained while growing a larger (3 nm) CdSe crown displays a clear redshift compared to the material presented in Figure 1.

The final material displays a bright yellow PL, see the inset of Figure 1d. XPS analysis of the material (Figure S2, Supporting Information) confirms the presence of Cd, Zn, S, and Se, which all mostly display a single contribution. The spectrum acquired around the S 2p state also overlaps with the Se 3p core levels. Despite the close cross-sections of 0.21 Mbarn for S 2p and 0.26 Mbarn for Se 3p at 700 eV,[32] the Se contribution appears only as a small shoulder in the spectrum (Figure S2d, Supporting Information), confirming the limited lateral extension of the CdSe crown. The transient absorption spectrum of the C–C–C structure displays similar features to those observed for CdSe core and CdS/CdSe core–crown structures, see **Figure 2**a. In particular, no bleach feature from CdS is observed, confirming that electrons and holes relax exclusively to the narrow CdSe crown as expected from a type I band alignment for the lateral interface.[33]

To gain further insights into the electronic properties of the heterostructure, we simulated the electron and hole densities of presence within the band edge exciton thanks to *k.p* simulation (see Experimental Section). We consider C–C–C NPLs with abrupt interfaces and the narrowest CdSe crown suggested by the chemical analysis (Figure S3, Supporting Information). This provides an upper limit on the potential influence of lateral confinement. As expected, the electron (Figure 2b) and hole (Figure S4, Supporting Information) are mostly located in the CdSe crown. However, the wave function does not acquire a ring shape. The in-plane anisotropic growth of the NPL makes the CdSe crown larger in the long direction of the NPL than in the perpendicular direction. As a result, the wave function tends to localize in this part of the ring instead of being homogeneously distributed all over the CdSe crown. This gives the heterostructure wave function the aspect of a diatomic molecule, with weak coupling between the two antinodes due to the CdS core acting as a tunnel barrier. The hole wave function (Figure S4, Supporting Information) presents an overall similar behavior, with a slightly more localized character due to the higher effective mass of holes with respect to electrons in II–VI semiconductors.

Modeling the spectrum of the heterostructure unveils a broad bandgap tunability of the CdSe through lateral confinement. Energy shifts above 400 meV are predicted, see **Figure 3**a, as the lateral extension of the CdSe crown is tuned over a range matching the CdSe Bohr radius. This shift seems robust toward a change in the electronic structure parameters used[34–39] (either tuning the effective mass or the conduction band offset between CdS and CdSe). However, the observed shift appears to be three times bigger than the one measured experimentally, a deviation that we connect to the actual distribution of selenium inside the NPL. Indeed, X-ray energy dispersive spectroscopy coupled with transmission electron microscopy (see Figure S3, Supporting Information) shows that selenium in the final product extends above the initial CdSe crown and in particular toward the external crown. This spread of the selenium beyond native design explains the broadening of the PL as well as the reduced spectral tunability. Size dispersion of the CdSe crown and emission from the wider crowns within an ensemble may play a role too.

To illustrate the spectral tunability, we have grown a series of samples, combining both in-plane (i.e., lateral confinement in the CdSe crown) and vertical (i.e., along the thickness) confinement, see Figure 3b. These samples exhibit bright emission with spectral tunability in the 500–650 nm range. In particular, materials with shells can address light emission at short wavelengths, through this strategy. The emission of these NPLs is not limited to visible photon excitation, as both cathodoluminescence (CL, i.e., electron excitation, see Figure S5a, Supporting Information) and radioluminescence (RL, i.e., excitation using X-ray, see Figure S5b, Supporting Information) have also been obtained and match the PL spectra. On the chromaticity diagram, the CL and RL spectra are slightly shifted to longer wavelengths compared to the PL spectra. This shift is expected, as high energy excitation is more likely to generate biexciton emission, as discussed in the next paragraph. The scintillation properties of the C–C–C CdS/CdSe/CdS samples are similar to CdSe nanoplatelets,[40,41] with light yields of 1 photon/keV or less, but with sharp emission peaks.

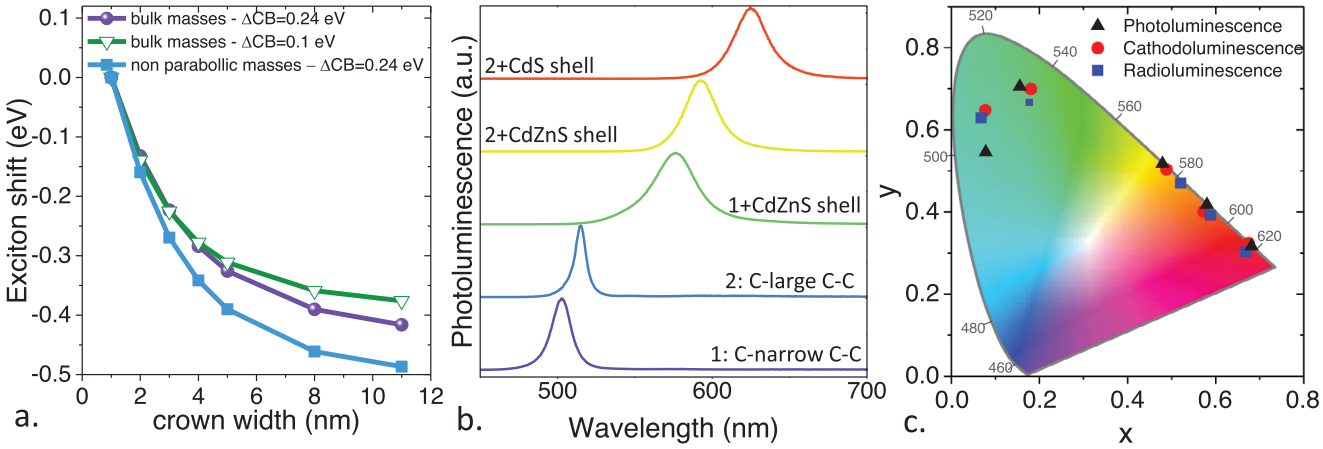

Figure 3. Spectral tunability and luminescence from CdS/CdSe/CdS C–C–C NPLs and their shelled counterparts. a) k.p simulated shifts of the band edge energy as a function of the CdSe crown extension. Three sets of material parameters have been used either using bulk effective masses with large (0.24 eV) or weak (0.1 eV) conduction band offsets between CdSe and CdS,[34–38] or using non-parabolic mass.[39] b) Photoluminescence spectra for CdS/CdSe/CdS C–C–C NPLs with a narrow (1 nm) CdSe crown (purple), for CdS/CdSe/CdS C–C–C NPLs with a large (3 nm) CdSe crown (blue), for CdS/CdSe/CdS/CdZnS C–C–C–S NPLs with a narrow (1 nm) CdSe crown (green), for CdS/CdSe/CdS/CdZnS C–C–C–S NPLs with a large (3 nm) CdSe crown (yellow), for CdS/CdSe/CdS/CdS C–C–C–S NPLs with a large (3 nm) CdSe crown (red). The excitation is set at 380 nm c) Chromaticity diagram showing the localization of the luminescence (PL, cathodoluminescence, and radioluminescence) for the five populations of NPL screened in part b.

We then tested the emission of this material under various incident powers to assess their potential for stimulated emission, see **Figure 4**. For C–C–C NPLs, as the incident power increases and switches from low (i.e., <1 exciton per NPL) to high excitation regimes (i.e., five excitons per NPL), we observe a clear broadening of the PL signal (Figure 4a). In particular, a new feature at ≈2.34 eV (530 nm) appears on the low-energy side of the PL peak. Its spectral shift compared to the exciton is of the order of 50 meV. This suggests that the second feature results from an attractive biexciton. Such a picture can be interpreted as an intermediate case between that of ideal C–C–C NPLs with narrow CdSe crowns and that of CdSe-only NPLs. In the former

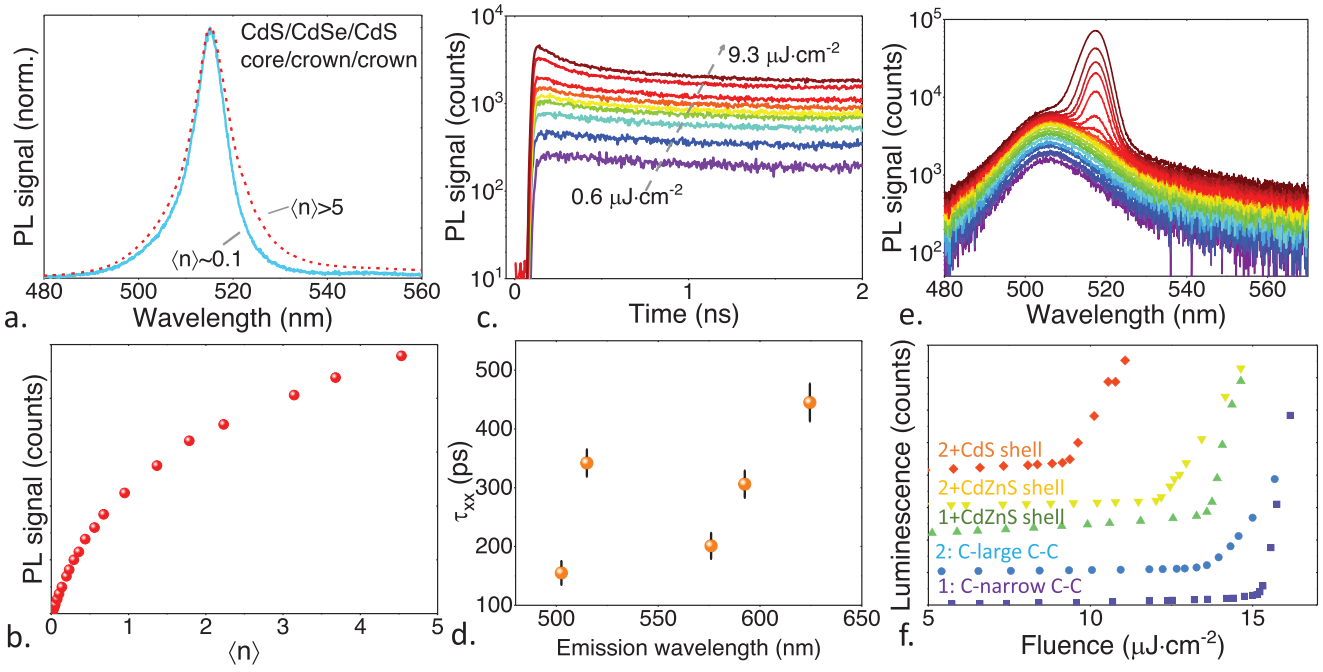

Figure 4. Biexciton and stimulated emission from CdS/CdSe/CdS C–C–C NPLs. a) Photoluminescence spectra under low (0.1 exciton per NPL) and high (five excitons per NPL) excitation. b) The magnitude of the integrated PL signal as a function of the incident power. c) Early-time transient PL signal under various excitation fluences. d) Bi-exciton lifetime for the same set of samples as for Figure 3b. e) Emission spectra from a stripe-illuminated sample with increasing excitation fluence. f) Photon counts with stripe illumination as a function of laser fluence for the same set of samples as in Figure 3b.

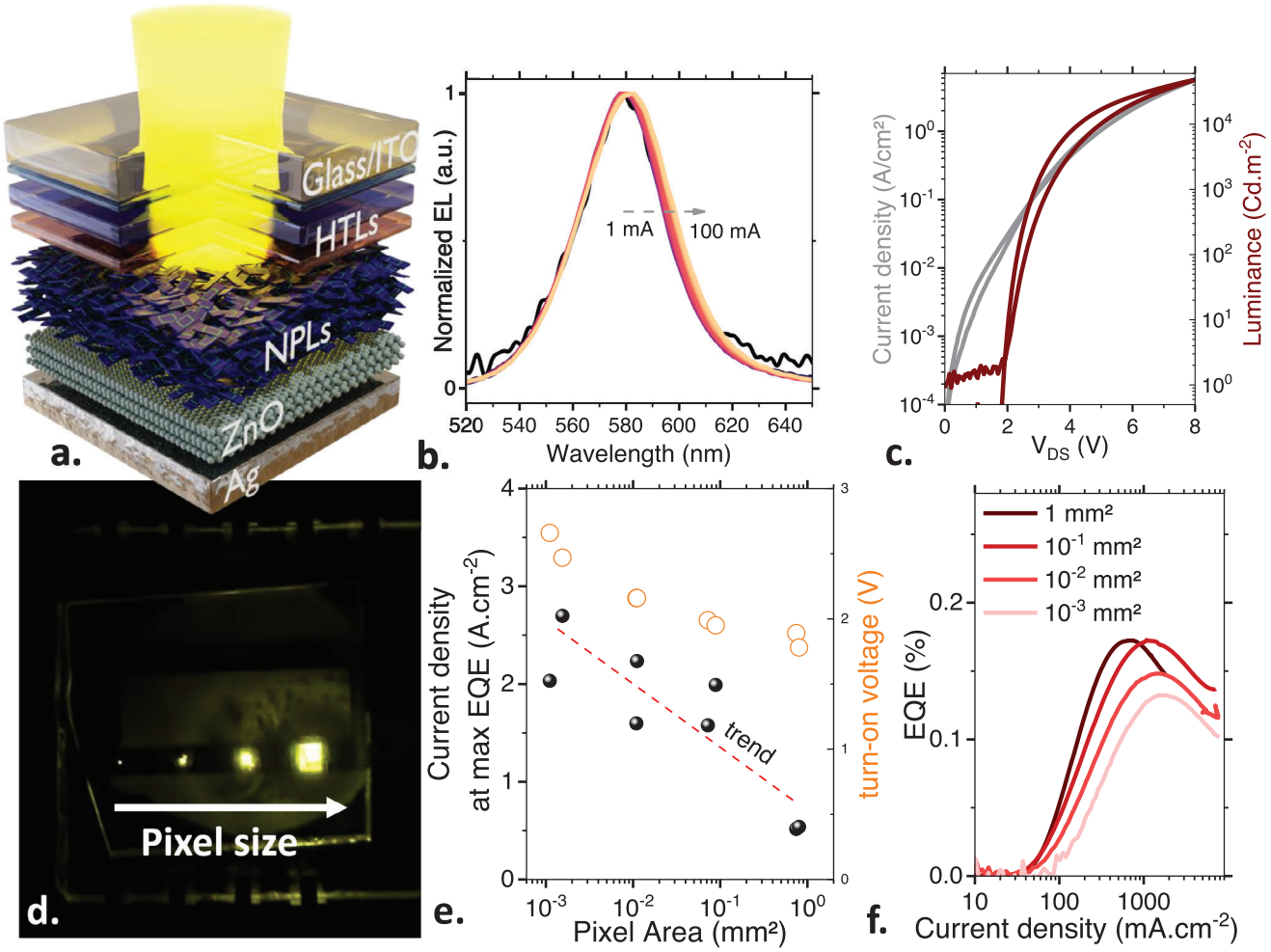

Figure 5. Electroluminescence from CdS/CdSe/CdS/CdZnS C–C–C–S NPLs. a) Schematic of the LED stack. b) EL spectra under various injection current. c) Current density and luminance as a function of the applied bias for a device with an area of 0.1 mm^2. d) Image of several pixels with different areas under operation. e) Current density at the maximum EQE and turn-on voltage as a function of the pixel area. f) EQE versus current density for four sizes of LED made from CdS/CdSe/CdS/CdZnS C–C–C–S.

case, the charge distribution is reminiscent of quasi-type-II structures, with electrons delocalized as compared to holes (cf. Figure 2 and Figure S4, Supporting Information). In order to reduce repulsive interactions, biexcitons in such systems are expected to localize one exciton on each side of the CdSe crown, separated by the inner CdS core. A weakly interacting biexciton is then formed, as in homodimer CdSe/CdS double quantum dots.[42] As the lateral confinement of the CdSe crown is relaxed, the NPL evolves toward the limit of a CdSe--only NPL, where attractive biexcitons have been confirmed both experimentally[43] and theoretically.[44]

As the power is increased, we observe a saturation of the PL signal magnitude (Figure 4b), which suggests the appearance of new non-radiative pathways likely resulting from Auger recombination. Time-resolved PL (Figure 4c) confirmed the emergence of a faster recombination mechanism under strong illumination. Normalizing all the data at a long-timescale allows the fit of the emerging fast contribution to extract a biexciton lifetime, which is in the 150–400 ps range for the series of samples under investigation, see Figure 4d. A biexciton lifetime of several hundred picoseconds is similar to previous findings of CdSe nanoplatelets.[8,45,46] We then used an fs-pulsed laser source to efficiently excite the biexciton luminescence and observe the emergence of a narrow feature on the low-energy side of the PL that increases non-linearly above a threshold fluence. The thresholds for the emergence of ASE are found in the 10–15 μJ cm^{-2} range, with a trend for reduced thresholds in materials grown with a shell, see Figure 4f. This is consistent with the larger size and therefore the greater absorptivity of the samples at the excitation wavelength with the growth of the shell, which allows a larger average number of excitons for the same input fluence.

Finally, we explore the potential to excite the luminescence of these NPLs through an electrical signal (i.e., electroluminescence: EL). To do so, the laterally confined C–C–C–S NPLs (material from Figure 1) are integrated into a diode stack schematized in **Figure** 5a, where organic polymers are used as hole injectors and ZnO nanoparticles as electron injectors.[47] Here, we focus on materials with a shell since stability is critical to maintaining

the luminescence while the material is exposed to the fabrication steps of the diode. Clearly, the drop in PL efficiency as the material is switched from a solution to a film is a clear bottleneck for core and core–crown NPLs.

Here, the material displays a bright yellow (580 nm or 2.13 eV) EL, see Figure 5b,d. As the injected current is increased, we observe a small redshift of the EL signal. However, the current density in the A.cm^{-2} range is too small to expect to generate population inversion, and the shift should be rather attributed to heating. In Figure S6 (Supporting Information), we tracked how the PL signal is affected by a change in temperature and found that the material shifts reversibly by 0.1 nm °C^{-1} and broadens by 0.06 nm °C^{-1}. The diode stack enables a low turn-on voltage at ≈2 V (Figure 5c), corresponding to a sub-bandgap operation. The luminance can be high, up to 4×10^4 Cd m^{-2}, with, however, a rather modest external quantum efficiency (EQE) of 0.2%, To understand the current limited EQE, it is worth pointing out that the resistance of this structure is actually smaller than the one obtained using the same stack based on CdSe/ZnS NPLs.[48] However, the latter presents a 5% EQE. The new structure being less resistive, the low EQE cannot be attributed to a charge injection issue though less favorable than in the initial design dedicated to red emitting quantum dots. In addition, the PLQY of the C–C–C–S structure is quite good at ≈68% in solution with no dramatic drop on film. Though the film is disordered, the relatively large-sized NPLs tend to lie flat and the overall projected surface of CdSe is low compared to core/shell structure. As a result, electron–hole pairs are injected but have a limited probability of recombining in the CdSe and up being radiative.

To limit the heating resulting from the Joule effect, we have reduced the pixel size and tracked the LED performances. Smaller pixels are obtained by introducing an alumina layer between the top and bottom electrode, with an opening whose size now defines the pixel size. We found that efficiency roll-offs shift to higher current densities with smaller pixel sizes. With less current passing overall in the device, the Joule effect is expected to be reduced. This points out that heating, in addition to the Auger recombinations that likely occurs at higher current densities, contributes significantly to the EQE roll-off, see Figure 5f. More surprisingly, we also observe that the turn-on voltage value can be affected (increasing from 1.8 V for a large pixel to 2.6 V for a small pixel, see Figure 5e) by the introduction of the dielectric layer, which funnels the current. This suggests that the electric field distribution is affected, possibly by fabrication or by current funneling effects, which is an underestimated effect and might be a problem for possible designs of single-photon emitter electrically pumped using colloidal nanocrystals.

3. Conclusion

We designed NPL heterostructures that combine both lateral and vertical quantum confinement. In particular, the synthetic strategy demonstrated here, in which lateral confinement can be finely tuned through the crown size, permits a much higher degree of control than otherwise achievable with the direct synthesis of nanoplatelets. By doing so, nanoparticles can combine the high stability brought by the shell together with an emission that is broadly tunable (with a theoretical limit of ≈400 meV). The material displays bright photoluminescence, radioluminescence, cathodoluminescence, and electroluminescence with high color saturation. Stimulated emission resulting from biexcitons has been demonstrated with a threshold at ≈10 μJ cm^{-2}. In light-emitting diodes, the downscaling of the pixel size appears to be a viable strategy to limit the heating damage resulting from the Joule effect. However, this downscaling also comes with more unexpected modifications of the LED internal electric field, suggesting that small diode devices may require specific optimization of the LED stack.

4. Experimental Section

Chemicals: Octadecene, ODE (Sigma–Aldrich, 90%), cadmium acetate anhydrous, $Cd(Ac)_2$ (Sigma–Aldrich, 99.995%), cadmium oxide, CdO (Strem 99.99%), zinc acetate dihydrate, $Zn(Ac)_2$ (Aldrich, 98%)), S powder (Sigma–Aldrich, 99.98%), Se powder (Strem Chemicals 99.99%), zinc acetate dihydrate (<97%, Alfa Aesar), tetramethylammonium hydroxide pentahydrate (TMAOH, 98%, Alfa Aesar), dimethyl sulfoxide (DMSO, ≥99.9%, Sigma–Aldrich), Lithium aluminum hydride (LiAlH4, Sigma–Aldrich, 95%), Sodium chloride (NaCl, Sigma–Aldrich, 99.0%), oleic acid, (OA, Sigma–Aldrich, 90%), decanoic acid (Sigma–Aldrich, 98%), stearoyl chloride (Sigma Aldrich, technical ≤ 90%), octanethiol (Fluka, 97%), oleylamine (OLA) (Acros, 80–90%), trioctylphosphine, TOP (Alpha Aesar, 90%), n-hexane (VWR, 99%), ethanol (VWR, 96%), methanol (VWR), toluene (VWR), diethyl ether (VWR), tetrahydrofuran (THF, anhydrous, Sigma–Aldrich). All chemicals were used as received.

TOP:S Precursor 1 M: In a glove box, 20 mL of TOP was mixed with 0.64 g of S powder (20 mmol). The mixture was stirred for a whole night and was then stored in the glove box.

TOP:Se Precursor 1 M: In a glove box, 20 mL of TOP was mixed with 1.58 g of Se powder(20 mmol). The mixture was stirred for a whole night and was then stored in the glove box.

Cadmium Decanoate (Cd(deca)$_2$) Precursor: In a 100 mL three-neck flask, 2 g of CdO (15.7 mmol) and 6.9 g of decanoic acid (40 mmol) were mixed and heated at 210 °C for 1 h under argon atmosphere. When the entire solid was dissolved and a colorless solution was obtained, the heating was stopped and acetone was added to precipitate cadmium decanoate. The powder was centrifugated and washed at least three times with acetone and then set under a vacuum overnight.

Bis(Stearoyl)Sulfide Precursor: In a 100 mL three-neck flask, 40 mL of dried THF was mixed with 139 mg of S powder (4.3 mmol) and cooled down to −10 °C using an ice bath filled with NaCl. One hundred forty-four milligrams of $LiAlH_4$ (3.8 mmol) was swiftly added and the system was put under Ar flux. A greyish color was observed. After 30 min, 1.36 mL of stearoyl chloride was added in 2 min. The operation at 60, 90, 120, and 150 min was repeated. The color went from yellowish to cream to white. Diethyl ether (50 mL) was added and washed five times with a saturated solution of NaCl. At this point, the mixture should be brown. Using a heat gun, the mixture was heated ≈50 °C until the solution became clear. And waited overnight for the crystallization. The solid was then filtered using a Büchner filter. The solid was kept under vacuum for the night and stored in a glovebox for further use.

Synthesis of CdS Core NPLs: In a three-neck flask, 136 mg of $Cd(deca)_2$ (0.3 mmol), 160 mg $Cd(Ac)_2{\bullet}2H_2O$ (0.6 mmol), 170 mg of bis(stearoyl)sulfide (0.3 mmol), and 15 mL of ODE was added. The mixture was degassed for 1 h at room temperature before switching the atmosphere to Ar. The temperature was then set at 190 °C. The reaction was followed by absorption and was stopped as soon as the features of the 3 ML CdS NPLs disappeared (c.a. 10 min). The NPLs were precipitated twice using a minimum of hexane and ethanol. The final pellet was redispersed in 15 mL of ODE (optical density of 0.53 at the excitonic peak for a solution diluted 100 times). This synthesis was adapted from ref. [49]

Synthesis of CdS/CdSe Core–Crown NPLs: In a three-neck flask, a whole synthesis of CdS 4 ML cores was mixed with 180 mg of $Cd(Ac)_2{\bullet}2H_2O$ (0.67 mmol) and 360 μL of OA. The mixture was degassed for 90 min

at 60 °C. The atmosphere was then switched to Ar and the temperature was set at 210 °C. When the temperature stabilized, 1.5 mL of TOP:Se (1 M diluted in ODE to reach a 0.05 M final concentration) was added at a 2 mL•h^{-1} injection flow. Ten minutes after the end of the addition, the reaction was cooled down to room temperature. The NPLs were then precipitated using a minimum of hexane and ethanol. The final pellet was redispersed in 15 mL of ODE.

Synthesis of CdS/CdSe/CdS C–C–C NPLs: In a three-neck flask, a whole synthesis of CdS-CdSe 4 ML core/crown NPLs was mixed with 180 mg of $Cd(Ac)_2$•$2H_2O$ (0.67 mmol) and 360 µL of OA. The mixture was degassed for 90 min at 60 °C. The atmosphere was then switched to Ar and the temperature was set at 210 °C. When the temperature stabilized, 2 mL of TOP:S (1 M diluted in ODE to reach a 0.1 M final concentration) was added at a 2 mL h^{-1} injection flow. Ten minutes after the end of the addition the reaction was cooled down to room temperature. The NPLs were then precipitated using a minimum of hexane and ethanol. The final pellet was redispersed in 15 mL of ODE.

Growth of the CdZnS shell: In a three-neck flask, a whole synthesis of CdS/CdSe/CdS C–C–C NPLs was mixed with 120 mg of $Cd_{0.05}Zn_{0.95}(Ac)_2$•$2H_2O$ (0.54 mmol, prepared by grinding $Cd(Ac)_2$•$2H_2O$ and $Zn(Ac)_2$•$2H_2O$), and 1 mL of OA. The mixture was degassed for 1 h at room temperature and then 30 min at 90 °C. The temperature was then set at 300 °C. At 120 °C, 1 mL of OLA was added. At 170 °C, the injection of 140 µL of octanethiol in 1 mL ODE at a 2.5 mL h^{-1} flow was started. When the temperature reached 280 °C, the injection flow was decreased at 1 mL h^{-1}. Wait an additional 30 min after the end of the injection. The NPLs were washed twice using a minimum of hexane and ethanol and were finally redispersed in toluene.

Absorption/PL Measurements: UV–vis spectra were acquired with a Cary 5000 spectrometer. Photoluminescence and excitation spectra were obtained with an Edinburgh instrument spectrometer. During the measurements, the NPLs were dispersed in hexane. For PL excitation measurements, care was taken to work in a diluted solution to limit emission reabsorption phenomena.

Time-Resolved Photoluminescence: Time-resolved photoluminescence of the samples was conducted in one of two ways. For nanosecond time-range time-resolved emission, a weak 375 nm pulsed laser diode (fluence <1 nJ cm^{-2}) was used to excite the samples in solution, with emission spectrally filtered using a monochromator and measured using a photon multiplier tube integrated into a fluorimeter (Edinburg). For fluence-dependent time-resolved photoluminescence, a 400 nm femtosecond pulse (Spectra physics, generated by second harmonic generation) was used to excite the samples in a solution with emission collected in free space and directed to a streak camera (Hamamatsu). The power of the 2 kHz pump was measured just before the sample and the spot size was measured using calibrated pinholes to estimate fluence. To estimate the cross-section of the samples, time-resolved data from the streak camera was collected for a fixed amount of time at each fluence (or photon flux), and the signal at long delay times (1.9–2 ns) was summed. The saturation of this signal depends on the cross-section of the samples according to $I_{PL}(j) = A(1 - e^{-\sigma j})$, where A is a scalar and j is the photon flux. Estimates of biexciton lifetime were obtained using previously established methods[50] to extract the two-exciton component from fluence-dependent data by subtracting the single-exciton component data apparent from normalization at long delay times after Auger recombination had occurred. The average number of excitons per particle for the extracted biexciton lifetimes was 0.2–0.3, in which the ensemble was dominated by particles with zero and one exciton and particles with two excitons represent a small fraction. Importantly, those with >2 excitons are exceedingly small.

Transient Absorption: Transient absorption was performed on selected samples dispersed in hexane solutions using the split output of a 2 kHz, 35 fs Ti: sapphire laser. The fundamental beam (800 nm) was split into pump and probe branches. The pump branch was upconverted to 400 nm excitation using a second harmonic generation crystal and chopped to 1 kHz; the probe branch was focused through a sapphire crystal to generate a visible supercontinuum white light. The pump and probe were spatially and temporally overlapped using an optical delay stage. The transient absorption signal was generated by comparison of the signal with and without the pump excitation.

Amplified Stimulated Emission: Amplified spontaneous emission (ASE) was measured using solid thin films of each sample deposited onto glass substrates. The samples were purified by washing with ethanol, then drop-cast onto glass treated with mercaptopropyltrimethoxy silane in toluene. Measurement of ASE was performed with a frequency-doubled Ti: sapphire laser (35 fs, 800 nm fundamental) operated at 200 Hz, which was focused onto the sample in a stripe with a height of 110 µm (measured by razor blade scan) and length of 3.8 mm. The emission from the samples was collected into a fiber at a right angle from the excitation and directed to a spectrometer. Fluence was obtained by measuring the power of the pump pulses just prior to hitting the sample.

Radioluminescence Spectroscopy: Radioluminescence spectroscopy was performed using a home-built copper k_α source directed onto solid films of samples, either deposited onto native oxide silicon or diluted into a polymer matrix. Collection of the emitted radioluminescence was performed with a collimating optic and fiber-coupled to an Andor spectrometer. Spectral collection was performed for 30 s.

Cathodoluminescence Spectroscopy: Cathodoluminescence spectroscopy was performed using a parabolic mirror and spectrometer (Delmic integration) on an FEI Quanta SEM. All data were collected with 5 keV accelerating voltage with 1 s integration. Measurements were performed on films drop-cast onto native oxide silicon chips.

Infrared Absorption Spectroscopy: For infrared spectroscopy, a ThermoFisher Nicolet iS50 was used in ATR (attenuated total reflection) mode. The spectra were averaged over 64 acquisitions and have a 4 cm^{-1} resolution. The light source was a halogen lamp, the beam splitter was CaF_2, and the detector was a DTGS sensor.

TEM: A drop of diluted NPLs solution was drop-casted onto a copper grid covered with an amorphous carbon film. The grid was degassed overnight under a secondary vacuum. Imaging was conducted using a JEOL 2010 transmission electron microscope operated at 200 kV. STEM-HAADF and EDX mapping were acquired with a ThermoFisher Spectra 200 TEM operated at 200 kV.

X-Ray Photoemission Measurements: Photoemission spectroscopy measurements are carried out at Tempo beamline of Synchrotron Soleil (France). Films of nanocrystals were spin-cast onto a gold-coated Si substrate (the gold layer was 80 nm thick). The films were dipped in methanol which acts as a ligand stripper. Samples were introduced in the preparation chamber and degassed until a vacuum below 10^{-9} mbar was reached. Then samples were introduced in the analysis chamber. The signal was acquired by a MBS A-1 photoelectron analyzer equipped with a delay line detector developed by Elettra synchrotron.[51] The acquisition was done at a constant pass energy (50 eV) within the detector. A photon energy of 700 eV was used for the analysis of the core levels. A gold substrate was used to calibrate the Fermi energy. The absolute value of the incoming photon energy was determined by measuring the first and second orders of Au 4f core level peaks. Then for a given analyzer pass energy, the Fermi edge was measured and its binding energy was set as zero. The same shift was applied to all spectra acquired with the same pass energy. The acquired core-level data were processed by subtracting a Shirley/linear background and pseudo-Voight function (20% weighted Lorentzian contribution) for peak fitting.

ZnO Synthesis for ETL: In a centrifuge tube, 0.75 g of $Zn(Ac)_2$•$2H_2O$ (3.4 mmol), were dissolved into 30 mL of DMSO. In a second centrifuge tube, 1 g of TMAOH (10.9 mmol) was dissolved into 10 mL of EtOH. The content of both tubes was quickly added into an Erlenmeyer flask under agitation by a magnetic stirrer. The mixture was then left to react at room temperature and under vigorous stirring for 24 h. After the reaction, the solution was transferred to a centrifuge tube, and ethyl acetate was added until precipitation occurred. The solution was then centrifuged at 6000 rpm for 3 min. The supernatant was discarded and the pellet was first dried and then redispersed in a minimum amount of ethanol absolute. Ethanolamine (320 µL) was added to stabilize the particles. Ethyl acetate was added until precipitation occurred and the solution was centrifuged at 6000 rpm for 3 min. The supernatant was discarded and the pellet was first dried and then redispersed in less than 4 mL of EtOH. The optical

density of the solution was measured at 350 nm to be 0.45 after a 300-times dilution.

ITO Patterning: ITO-coated glass substrates (30 Ω sq^{-1} from Solem) were cut into 15 mm × 15 mm pieces and cleaned by sonication in acetone for 5 min. After sonication, the substrates were rinsed with acetone and isopropanol before being dried completely with N_2 flow. The substrates were further cleaned with O_2 plasma for 5 min to remove organic residuals on the surface. After cleaning, TI-Prime and AZ 5214E photoresists were sequentially spin-coated on the surface of ITO substrates at the rate of 4000 rpm for 30 s and baked at 110 °C for 120 and 90 s, respectively. A mask aligner was then used to expose the substrates to UV light for 20 s through a lithography mask (1 mm width). The photoresist was then developed using AZ 726 developer for 20 s before rinsing with deionized water and drying with N_2 flux. After another 5 min plasma cleaning, the substrates were etched in a 25% HCl (in water) bath for 10 min at 40 °C before they were dipped immediately in deionized water. Finally, the lift-off was conducted in an acetone bath. Before being used, the patterned ITO substrates were cleaned with acetone and isopropanol first and put under plasma for 10 min.

Alumina Patterning to Define Small Pixel: On top of the patterned ITO, Alumina (Al_2O_3) was deposited via 450 cycles of atomic layer deposition (ALD) from trimethylaluminum and water as precursors, for a total thickness of 40 nm. Openings in the alumina layer were then made using optical lithography and acid etching. After cleaning the substrate with O_2 plasma, TI-Prime and AZ 5214E photoresist were sequentially spin-coated on the surface of ITO substrates at the rate of 4000 rpm for 30 s and baked at 110 °C for 120 and 90 s, respectively. A mask aligner was then used to expose the substrates to UV light for 1.5 s through a lithography mask that defines square openings of varying widths on top of the ITO. The substrate was then baked at 129 °C in order to invert the resist. The substrate was exposed again to UV light for 40 s, without any mask. The resist was developed using a bath of AZ726 for 30 s, rinsed in pure water, and dried with N_2. Then, the alumina was etched by an H_3PO_4 (85%) solution at 50 °C for 6 min. Finally, the lift-off was conducted in an acetone bath.

LED Fabrication: A PEDOT:PSS solution (filtered through 0.45 µm filter) was spin-coated on a thoroughly cleaned patterned Alumina/ITO/Glass substrate at 4000 rpm for 60 s and annealed at 140 °C for 10 min in air. Inside a Nitrogen-filled glovebox, 4-Butyl-*N*,*N*-diphenylaniline homopolymer (Poly-TPD at 8 mg mL^{-1} in chlorobenzene), Poly(9-vinylcarbazole (PVK at 1.5 mg mL^{-1} in m-xylene), NPLs and ZnO nanoparticles were successively spin-coated at 2000 rpm for 45 s on the PEDOT: PSS-coated substrate. After the deposition of Poly-TPD, the sample was annealed at 110 °C for 20 min. After the deposition of PVK, the sample was annealed at 170 °C for 30 min. Finally, 80 nm of Ag was deposited on top of the ZnO using a shadow mask by thermal evaporation. The devices were encapsulated inside the glove box with a piece of glass by Ossila E132 Encapsulation Epoxy. The overlap between the ITO not covered with alumina and Ag defines the pixel area.

Electroluminescence Spectra: Electroluminescence spectra were collected by a Flame Spectrometer equipped with a Si detector from Ocean Optics while passing a constant current with a Keithley 2400.

LED Characterization: For characterization,current–voltage–power characteristics were collected with a Keithley K2634B source-meter unit and a PM100A power-meter coupled with the S120C Si detector from Thorlabs. EQE, irradiance, and luminance values were derived from these measurements through calculations. Considering the Lambertian emission of an LED device, the flux leaving the device can be described as $F_{ext} = \int_0^{\pi/2} 2\pi L_0 \cos\theta \sin\theta d\theta = \pi L_0$, with L_0 the flux per solid angle of light leaving the device in the forward direction. Since the solid angle from the photodetector to the light source is $\Omega = \frac{S_1}{l^2}$ with S_1 the area of the detector and l the distance between the light source and detector, then $L_0 = \frac{P_{det}}{\Omega} = \frac{P_{det} l^2}{s_1}$ and $F_{ext} = \frac{\pi P_{det} l^2}{s_1}$. The number of photons emitted per second to the forward direction can then be calculated by $N_P = \frac{F_{ext}}{h\nu} = \frac{\pi P_{det} l^2 \lambda}{s_1 hc}$, with λ the wavelength of electroluminescence, h the Plank's constant, and c the speed of light. The number of electrons injected per second can be obtained by $N_P = \frac{I}{e}$, with I the current flow of the device. Thus, the EQE can be calculated as $EQE = \frac{N_p}{N_e} = \frac{\pi P_{det} l^2 \lambda e}{s_1 hcI}$. The irradiance of the device is $R = \frac{F_{ext}}{s_2} = \frac{\pi P_{det} l^2}{s_1 s_2}$, with S_2 the area of the pixel. The luminance of the device is $L = \frac{683 * V(\lambda) * F_{ext}}{\pi * s_2} = \frac{683 * V(\lambda) * P_{det} * l^2}{s_1 s_2}$, with $V(\lambda)$ being the function of photonic eye sensitivity and $V(\lambda) \approx 0.87$ for $\lambda = 580\ nm$. Knowing that the working diameter of the detector area was 9.5 mm and assuming the distance between detector and device to be 6.5 mm in this case, the geometry-related value of $\Omega = \frac{S_1}{l^2}$ was ≈1.68 in the setup.

k·p Modeling: Electron and heavy hole states were calculated with single-band k·p Hamiltonians. These include self-energy terms arising from the dielectric mismatch with the organic medium, as well as strain arising from the lattice mismatch between the core, the crowns, and the shell. The strain was obtained within the continuum elastic approximation. Excitonic interactions were accounted for with a self-consistent calculation, where Coulomb integrals were obtained by integrating the Poisson equation in a dielectrically inhomogeneous system, see Supporting Information of ref. [15] for details of the model and material parameters of CdSe and CdS. Material parameters for the CdZnS shell were taken as an average from those of CdS and those of ZnS (all of them taken from ref. [52] except deformation potentials (from ref. [53]) and band offsets (from ref. [54])). Conduction band offsets turn out to be 0.24 eV for CdSe/CdS, and 0.65 eV for CdSe/CdZnS. Valence band offsets were −0.48 eV for CdSe/CdS and −0.73 eV for CdSe/CdZnS. The relative dielectric constant was taken to be 10 inside the NPL (roughly the mean value of the different metal chalcogenides in the NPL) and 2.0 outside, which is a typical value for organic ligands. The calculations correspond to CdS/CdSe/CdS NPLs with 4.5 monolayer (MLs) thickness, coated with 2 MLs of CdZnS on top and bottom. Following TEM data for a typical reference sample, the CdS core was taken with dimensions 7.5 × 12 nm^2, the CdSe crown 8.5 × 14 $nm^2$and the external CdS crown 12 × 32 nm^2. The CdZnS shell had the same lateral dimensions as the external CdS crown. To study the effect of the CdSe crown size, lateral dimensions were increased from (Lx,Ly) = (8.5,14) nm to (18.5,24) nm. The dimensions of the external CdS crown were increased by the same amount.

Supporting Information

Supporting Information is available from the Wiley Online Library or from the author.

Acknowledgements

L.C. and C.D. contributed equally to this work. J.I.C. acknowledges support from grant no. PID2021-128659NB-I00, funded by Ministerio de Ciencia e Innovación (MCIN/AEI/10.13039/501100011033 and ERDF A way of making Europe). The project was supported by ERC grant Ne2Dem (grant no. 853049) and AQDtive (grant no.101086358). The authors acknowledge the use of clean-room facilities from the "Centrale de Proximité Paris-Centre" and support from Renatech for micro and nanofabrication. This work was supported by French state funds managed by the ANR through the grants Frontal (ANR-19-CE09-0017), Graskop (ANR-19-CE09-0026), Copin (ANR-19-CE24-0022), Bright (ANR-21-CE24-0012-02), MixDferro (ANR-21-CE09-0029), Operatwist (ANR-22-CE09-0037-01) and E-map (ANR-23-CE50). Work performed at the Center for Nanoscale Materials and Advanced Photon Source, both U.S. Department of Energy Office of Science User Facilities, was supported by the U.S. DOE, Office of Basic Energy Sciences, under Contract No. DE-AC02-06CH11357.

Conflict of Interest

The authors declare no conflict of interest.

Data Availability Statement

The data that support the findings of this study are available from the corresponding author upon reasonable request.

Keywords

2D materials, luminescence, nanoplatelets, quantum confinement

Received: February 27, 2024
Revised: May 21, 2024
Published online:

[1] H. A. Nguyen, G. Dixon, F. Y. Dou, S. Gallagher, S. Gibbs, D. M. Ladd, E. Marino, J. C. Ondry, J. P. Shanahan, E. S. Vasileiadou, S. Barlow, D. R. Gamelin, D. S. Ginger, D. M. Jonas, M. G. Kanatzidis, S. R. Marder, D. Morton, C. B. Murray, J. S. Owen, D. V. Talapin, M. F. Toney, B. M. Cossairt, *Chem. Rev.* **2023**, *123*, 7890.
[2] M. Nasilowski, B. Mahler, E. Lhuillier, S. Ithurria, B. Dubertret, *Chem. Rev.* **2016**, *116*, 10934.
[3] J. Zhang, Y. Sun, S. Ye, J. Song, J. Qu, *Chem. Mater.* **2020**, *32*, 9490.
[4] B. T. Diroll, B. Guzelturk, H. Po, C. Dabard, N. Fu, L. Makke, E. Lhuillier, S. Ithurria, *Chem. Rev.* **2023**, *123*, 3543.
[5] A. Riedinger, F. D. Ott, A. Mule, S. Mazzotti, P. N. Knüsel, S. J. P. Kress, F. Prins, S. C. Erwin, D. J. Norris, *Nat. Mater.* **2017**, *16*, 743.
[6] N. Moghaddam, C. Dabard, M. Dufour, H. Po, X. Xu, T. Pons, E. Lhuillier, S. Ithurria, *J. Am. Chem. Soc.* **2021**, *143*, 1863.
[7] B. Guzelturk, Y. Kelestemur, M. Olutas, S. Delikanli, H. V. Demir, *ACS Nano* **2014**, *8*, 6599.
[8] C. She, I. Fedin, D. S. Dolzhnikov, P. D. Dahlberg, G. S. Engel, R. D. Schaller, D. V. Talapin, *ACS Nano* **2015**, *9*, 9475.
[9] J. Yu, M. Sharma, M. Li, S. Delikanli, A. Sharma, M. Taimoor, Y. Altintas, J. R. McBride, T. Kusserow, T.-C. Sum, H. V. Demir, C. Dang, *Laser Photonics Rev.* **2021**, *15*, 2100034.
[10] S. Ithurria, M. D. Tessier, B. Mahler, R. P. S. M. Lobo, B. Dubertret, A. L. Efros, *Nat. Mater.* **2011**, *10*, 936.
[11] S. Christodoulou, J. I. Climente, J. Planelles, R. Brescia, M. Prato, B. Martín-García, A. H. Khan, I. Moreels, *Nano Lett.* **2018**, *18*, 6248.
[12] W. Cho, S. Kim, I. Coropceanu, V. Srivastava, B. T. Diroll, A. Hazarika, I. Fedin, G. Galli, R. D. Schaller, D. V. Talapin, *Chem. Mater.* **2018**, *30*, 6957.
[13] A. Chu, C. Livache, S. Ithurria, E. Lhuillier, *J. Appl. Phys.* **2018**, *123*, 035701.
[14] S. Pedetti, S. Ithurria, H. Heuclin, G. Patriarche, B. Dubertret, *J. Am. Chem. Soc.* **2014**, *136*, 16430.
[15] A. V. Antanovich, A. V. Prudnikau, D. Melnikau, Y. P. Rakovich, A. Chuvilin, U. Woggon, A. W. Achtstein, M. V. Artemyev, *Nanoscale* **2015**, *7*, 8084.
[16] A. Sharma, M. Sharma, K. Gungor, M. Olutas, D. Dede, H. V. Demir, *Adv. Opt. Mater.* **2019**, *7*, 1900831.
[17] M. Dufour, E. Izquierdo, C. Livache, B. Martinez, M. G. Silly, T. Pons, E. Lhuillier, C. Delerue, S. Ithurria, *ACS Appl. Mater. Interfaces* **2019**, *11*, 10128.
[18] A. H. Khan, V. Pinchetti, I. Tanghe, Z. Dang, B. Martín-García, Z. Hens, D. Van Thourhout, P. Geiregat, S. Brovelli, I. Moreels, *Chem. Mater.* **2019**, *31*, 1450.
[19] N. Saenz, L. S. Hamachi, A. Wolock, B. H. Goodge, A. Kuntzmann, B. Dubertret, I. Billinge, L. F. Kourkoutis, D. A. Muller, A. C. Crowther, J. S. Owen, *Chem. Sci.* **2023**, *14*, 12345.
[20] E. Izquierdo, A. Robin, S. Keuleyan, N. Lequeux, E. Lhuillier, S. Ithurria, *J. Am. Chem. Soc.* **2016**, *138*, 10496.
[21] Y. Kelestemur, B. Guzelturk, O. Erdem, M. Olutas, K. Gungor, H. V. Demir, *Adv. Funct. Mater.* **2016**, *26*, 3570.
[22] S. Delikanli, B. Canimkurbey, P. L. Hernández-Martínez, F. Shabani, A. T. Isik, I. Ozkan, I. Bozkaya, T. Bozkaya, F. Isik, E. G. Durmusoglu, M. Izmir, H. Akgun, H. V. Demir, *J. Am. Chem. Soc.* **2023**, *145*, 12033.
[23] X. Liang, E. G. Durmusoglu, M. Lunina, P. L. Hernandez-Martinez, V. Valuckas, F. Yan, Y. Lekina, V. K. Sharma, T. Yin, S. T. Ha, Z. X. Shen, H. Sun, A. Kuznetsov, H. V. Demir, *ACS Nano* **2023**, *17*, 19981.
[24] F. Shabani, P. L. H. Martinez, N. Shermet, H. Korkut, I. Sarpkaya, H. Dehghanpour Baruj, S. Delikanli, F. Isik, E. G. Durmusoglu, H. V. Demir, *Small* **2023**, *19*, 2205729.
[25] A. H. Khan, G. H. V. Bertrand, A. Teitelboim, C. Sekhar, M. A. Polovitsyn, R. Brescia, J. Planelles, J. I. Climente, D. Oron, I. Moreels, *ACS Nano* **2020**, *14*, 4206.
[26] C. Dabard, V. Guilloux, C. Gréboval, H. Po, L. Makke, N. Fu, X. Z. Xu, M. G. Silly, G. Patriarche, E. Lhuillier, T. Barisien, J. I. Climente, B. T. Diroll, S. Ithurria, *Nat. Commun.* **2022**, *13*, 5094.
[27] C. Dabard, H. Po, N. Fu, L. Makke, H. Lehouelleur, L. Curti, X. Z. Xu, E. Lhuillier, B. T. Diroll, S. Ithurria, *Nanoscale* **2023**, *15*, 14651.
[28] B. T. Diroll, I. Fedin, P. Darancet, D. V. Talapin, R. D. Schaller, *J. Am. Chem. Soc.* **2016**, *138*, 11109.
[29] D. Schooss, A. Mews, A. Eychmüller, H. Weller, *Phys. Rev. B* **1994**, *49*, 17072.
[30] J. Beavon, J. Huang, D. Harankahage, M. Montemurri, J. Cassidy, M. Zamkov, *Chem. Commun.* **2023**, *59*, 11337.
[31] D. Harankahage, J. Cassidy, J. Beavon, J. Huang, N. Brown, D. B. Berkinsky, A. Marder, B. Kayira, M. Montemurri, P. Anzenbacher, R. D. Schaller, L. Sun, M. G. Bawendi, A. V. Malko, B. T. Diroll, M. Zamkov, *J. Am. Chem. Soc.* **2023**, *145*, 13326.
[32] J. J. Yeh, I. Lindau, *At Data Nucl Data Tables* **1985**, *32*, 1.
[33] M. D. Tessier, P. Spinicelli, D. Dupont, G. Patriarche, S. Ithurria, B. Dubertret, *Nano Lett.* **2014**, *14*, 207.
[34] C. Grivas, C. Li, P. Andreakou, P. Wang, M. Ding, G. Brambilla, L. Manna, P. Lagoudakis, *Nat. Commun.* **2013**, *4*, 2376.
[35] D. Steiner, D. Dorfs, U. Banin, F. Della Sala, L. Manna, O. Millo, *Nano Lett.* **2008**, *8*, 2954.
[36] A. Sitt, F. D. Sala, G. Menagen, U. Banin, *Nano Lett.* **2009**, *9*, 3470.
[37] G. Rainò, T. Stöferle, I. Moreels, R. Gomes, J. S. Kamal, Z. Hens, R. F. Mahrt, *ACS Nano* **2011**, *5*, 4031.
[38] J. Müller, J. M. Lupton, P. G. Lagoudakis, F. Schindler, R. Koeppe, A. L. Rogach, J. Feldmann, D. V. Talapin, H. Weller, *Nano Lett.* **2005**, *5*, 2044.
[39] R. Benchamekh, N. A. Gippius, J. Even, M. O. Nestoklon, J.-M. Jancu, S. Ithurria, B. Dubertret, A.l. L. Efros, P. Voisin, *Phys. Rev. B* **2014**, *89*, 035307.
[40] R. M. Turtos, S. Gundacker, S. Omelkov, B. Mahler, A. H. Khan, J. Saaring, Z. Meng, A. Vasil'ev, C. Dujardin, M. Kirm, I. Moreels, E. Auffray, P. Lecoq, *NPJ 2D Mater Appl* **2019**, *3*, 37.
[41] Z. Meng, B. Mahler, J. Houel, F. Kulzer, A. Vasil'ev, C. Dujardin, *Mater. Adv.* **2022**, *3*, 8341.
[42] N. Frenkel, E. Scharf, G. Lubin, A. Levi, Y. E. Panfil, Y. Ossia, J. Planelles, J. I. Climente, U. Banin, D. Oron, *ACS Nano* **2023**, *17*, 14990.
[43] F. G. Flórez, L. D. A. Siebbeles, H. T. C. Stoof, *Phys. Rev. B* **2020**, *102*, 115302.
[44] D. F. Macias-Pinilla, J. Planelles, J. I. Climente, *Nanoscale* **2022**, *14*, 8493.
[45] Q. Li, T. Lian, *Nano Lett.* **2017**, *17*, 3152.
[46] J. P. Philbin, A. Brumberg, B. T. Diroll, W. Cho, D. V. Talapin, R. D. Schaller, E. Rabani, *J. Chem. Phys.* **2020**, *153*, 054104.
[47] X. Dai, Z. Zhang, Y. Jin, Y. Niu, H. Cao, X. Liang, L. Chen, J. Wang, X. Peng, *Nature* **2014**, *515*, 96.

[48] J. Qu, P. Rastogi, C. Gréboval, C. Livache, M. Dufour, A. Chu, S.-S. Chee, J. Ramade, X. Z. Xu, S. Ithurria, E. Lhuillier, *ACS Appl. Mater. Interfaces* **2020**, *12*, 22058.
[49] A. Antanovich, L. Yang, S. C. Erwin, B. Martín-García, R. Hübner, C. Steinbach, D. Schwarz, N. Gaponik, V. Lesnyak, *Chem. Mater.* **2022**, *34*, 10361.
[50] V. I. Klimov, A. A. Mikhailovsky, D. W. McBranch, C. A. Leatherdale, M. G. Bawendi, *Science* **2000**, *287*, 1011.
[51] N. Bergeard, M. G. Silly, D. Krizmancic, C. Chauvet, M. Guzzo, J. P. Ricaud, M. Izquierdo, L. Stebel, P. Pittana, R. Sergo, G. Cautero, G. Dufour, F. Rochet, F. Sirotti, *J Synchrotron Radiat* **2011**, *18*, 245.
[52] S. Adachi, *Handbook on Physical Properties of Semiconductors*, Springer Science & Business Media, Berlin, **2004**.
[53] Y.-H. Li, X. G. Gong, S.-H. Wei, *Phys. Rev. B* **2006**, *73*, 245206.
[54] Y.-H. Li, A. Walsh, S. Chen, W.-J. Yin, J.-H. Yang, J. Li, J. L. F. Da Silva, X. G. Gong, S.-H. Wei, *Appl. Phys. Lett.* **2009**, *94*, 212109.